



# McrD binds asymmetrically to methyl-coenzyme M reductase improving active-site accessibility during assembly

Grayson L. Chadwick<sup>a,1,2</sup> , Aaron M. N. Joiner<sup>a,1</sup> , Sangeetha Ramesh<sup>b,c</sup> , Douglas A. Mitchell<sup>b,c,d</sup> , and Dipti D. Nayak<sup>a,2</sup>

Edited by Amy Rosenzweig, Northwestern University, Evanston, IL; received February 17, 2023; accepted May 4, 2023

Methyl-coenzyme M reductase (MCR) catalyzes the formation of methane, and its activity accounts for nearly all biologically produced methane released into the atmosphere. The assembly of MCR is an intricate process involving the installation of a complex set of posttranslational modifications and the unique Ni-containing tetrapyrrole called coenzyme F<sub>430</sub>. Despite decades of research, details of MCR assembly remain largely unresolved. Here, we report the structural characterization of MCR in two intermediate states of assembly. These intermediate states lack one or both F<sub>430</sub> cofactors and form complexes with the previously uncharacterized McrD protein. McrD is found to bind asymmetrically to MCR, displacing large regions of the alpha subunit and increasing active-site accessibility for the installation of F<sub>430</sub>—shedding light on the assembly of MCR and the role of McrD therein. This work offers crucial information for the expression of MCR in a heterologous host and provides targets for the design of MCR inhibitors.

methanogenesis | archaea | cryo-EM | methane | metalloenzyme

Methyl-coenzyme M reductase (MCR) is the enzyme responsible for nearly all biological methane production and is found exclusively in the domain archaea. MCR is a C<sub>2</sub>-symmetric heterohexamer defined by  $\alpha_2\beta_2\gamma_2$  subunit stoichiometry (*SI Appendix, Fig. S1A*). Substrate tunnels lined with posttranslational modifications (PTMs) end in two active sites formed at the interface of the  $\alpha$ ,  $\alpha'$ ,  $\beta$ , and  $\gamma$  subunits and  $\alpha'$ ,  $\alpha$ ,  $\beta'$ , and  $\gamma'$  on the opposing side (*SI Appendix, Fig. S1 B and C*). Each active site contains F<sub>430</sub>, a unique Ni porphinoide that catalyzes the reduction of methyl-coenzyme M (CH<sub>3</sub>-CoM) by coenzyme B (CoB), yielding methane and a heterodisulfide (1) (*SI Appendix, Fig. S1D*). Subsequent studies have determined MCR structures from diverse methanogens (2, 3); mutants lacking specific substrate channel PTMs (4, 5); anaerobic methanotrophic (ANME) archaea, which use the enzyme in the reverse direction for methane oxidation (6); and the recently discovered alkyl-coenzyme M reductases, which can oxidize short chain alkanes (7). Together, this research has facilitated studies on the reaction mechanism of MCR (8), and the mode of action for MCR inhibitors used to reduce the emission of this potent greenhouse gas (9, 10).

Despite the advances in our understanding of MCR structure and function, key questions regarding its assembly and activation remain unresolved. For instance, the three subunits  $\alpha\beta\gamma$  encoded by the *mcrABG* genes are usually found together in an operon with two additional genes: *mcrC* and *mcrD* (Fig. 1A). The function of the McrC and McrD proteins is unknown, but they are universally conserved in methanogens and have been suggested to be involved in MCR activation (11) and assembly (12), respectively. McrD associates with MCR in native organisms (13) and when heterologously expressed (12, 14), and McrD produced in *E. coli* stimulated the final step of F<sub>430</sub> biosynthesis (15). Based on these observations, McrD is hypothesized to be a chaperone required for the insertion of F<sub>430</sub> into a previously unobserved apo-MCR (12, 16). Here, we utilize Cas9-based genome editing in *Methanosarcina acetivorans* (17) to characterize McrD and employ single-particle cryo-electron microscopy (cryo-EM) to visualize McrD-bound MCR assembly intermediates.

## Results

Surprisingly, although the entire MCR operon is essential (18), the *mcrD* gene is not in *M. acetivorans* (Fig. 1A). We generated a  $\Delta mcrD$  mutant and verified the absence of compensatory mutations or off-target editing by whole-genome resequencing (*SI Appendix, Fig. S2*). This  $\Delta mcrD$  strain exhibited only a minor increase in doubling time compared to the parental strain (WWM60; also referred to here as wild type or WT) when grown on a variety of substrates (Fig. 1B). The growth defect remained negligible in cells stressed by nickel limitation, oxygen exposure, and nonideal growth temperatures (*SI Appendix, Fig. S3*). Consistent with this minor growth defect, only a small number of genes were significantly

## Significance

Methane is the second largest contributor to climate change with a warming potential substantially greater than carbon dioxide. Reducing methane emissions is crucial to meet climate goals. A significant portion of methane comes from methanogenic archaea through the action of an enzyme called methyl-coenzyme M reductase (MCR). Methane emissions can be drastically reduced by inhibiting the assembly or activity of MCR. Here, we provide a glimpse into the mechanism of MCR assembly in the model methanogen, *Methanosarcina acetivorans*. We show that McrD, a universally conserved protein in methanogens, facilitates the insertion of F<sub>430</sub>, a Ni-containing tetrapyrrole used by MCR for catalysis. Ultimately, these insights will facilitate translational research to design robust measures for global methane mitigation.

Author contributions: G.L.C. and D.D.N. designed research; G.L.C., A.M.N.J., and S.R. performed research; G.L.C., A.M.N.J., S.R., D.A.M., and D.D.N. contributed new reagents/analytic tools; G.L.C., A.M.N.J., S.R., and D.A.M. analyzed data; and G.L.C., A.M.N.J., S.R., D.A.M., and D.D.N. wrote the paper.

The authors declare no competing interest.

This article is a PNAS Direct Submission.

Copyright © 2023 the Author(s). Published by PNAS. This open access article is distributed under [Creative Commons Attribution-NonCommercial-NoDerivatives License 4.0 \(CC BY-NC-ND\)](https://creativecommons.org/licenses/by-nc-nd/4.0/).

<sup>1</sup>G.L.C. and A.M.N.J. contributed equally to this work.

<sup>2</sup>To whom correspondence may be addressed. Email: chadwick@berkeley.edu or dnayak@berkeley.edu.

This article contains supporting information online at <https://www.pnas.org/lookup/suppl/doi:10.1073/pnas.2302815120/-/DCSupplemental>.

Published June 12, 2023.

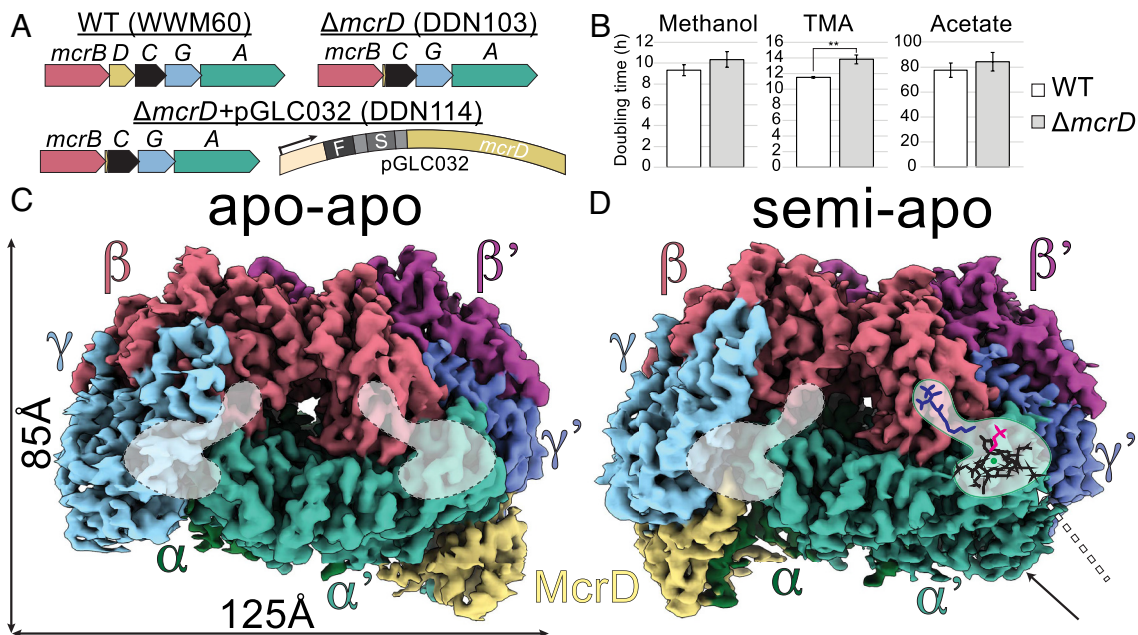


**Fig. 1.** Construction of  $\Delta mcrD$  strain and cryo-EM structure of McrD-bound MCR complexes. (A) MCR operon in the parental strain (WWM60),  $\Delta mcrD$  mutant (DDN103), and tagged complementation strain (DDN114). Arrow indicates pMcrB(tetO1) promoter used for tetracycline-inducible expression of McrD. F and S represent FLAG and Strep tags, respectively. (B) Doubling times of WT and  $\Delta mcrD$  strain on methanol (MeOH), trimethylamine (TMA), and acetate (\*\**P*-value < 0.01, two-sided *t* test). (C and D) Cryo-EM densities of the apo-apo and semi-apo McrABGD complexes (SI Appendix, Table S4). Empty active sites are outlined with dotted lines, while filled active site on the contralateral side of the semi-apo model is indicated by the dashed arrow. Solid arrow indicates density corresponding to the N-terminal domain of the  $\alpha'$  subunit in the semi-apo complex that is absent in the apo-apo complex.

differentially expressed in the  $\Delta mcrD$  mutant (SI Appendix, Fig. S4). Because McrD was hypothesized to be involved in the insertion of  $F_{430}$ , we assessed the relative amount of  $F_{430}$  loaded into MCR in the  $\Delta mcrD$  mutant as compared to the parent strain. An equivalent amount of MCR from the  $\Delta mcrD$  mutant exhibited only ~36% of the  $F_{430}$  absorbance present in MCR from WT (SI Appendix, Fig. S5). This observation lends support to the hypothesis that McrD plays a role in loading  $F_{430}$  in MCR. Additionally, a decrease in the abundance of functional MCR might be responsible for the minor growth defect observed in the  $\Delta mcrD$  mutant (Fig. 1B).

To understand more about McrD's potential role in  $F_{430}$  loading, we used a tetracycline-inducible expression vector to reintroduce the *mcrD* gene with N-terminal tandem FLAG and Strep tags into the  $\Delta mcrD$  background (Fig. 1A). McrD expression was verified by western blot against the FLAG epitope in crude cell extracts (SI Appendix, Fig. S6). Affinity purification of tagged McrD yielded stoichiometric amounts of McrA, B, and G subunits, indicative of a McrABGD complex in *M. acetivorans* (SI Appendix, Fig. S7). This complex is less thermostable and exhibited far less  $F_{430}$  absorbance compared to full assembled MCR (19) (SI Appendix, Fig. S8). Intriguingly, this complex could only be recovered from actively dividing cells, while purification from cells in stationary phase yielded predominantly free McrD (SI Appendix, Fig. S7). The presence of an McrABGD complex primarily in exponential phase is consistent with its role in the assembly of MCR rather than in a repair pathway to salvage damaged MCR. Additionally, isolation of the McrABGD complex was insensitive to the location of affinity tags on McrD, suggesting that it forms through a biologically relevant interaction between McrD and the other subunits, not a spurious interaction between the tag and MCR (SI Appendix, Fig. S7).

Two distinct conformational states of the McrABGD complex were discovered by cryo-EM: 1) semi-apo at 3Å and 2) apo-apo at 3.1Å (Fig. 1 C and D and SI Appendix, Figs. S9 and S10). We docked a previous crystal structure, of the MCR<sub>oxl-silent</sub> state purified from *Methanosarcina barkeri* (2), along with an AlphaFold2

(20, 21) prediction of McrD into both densities and then manually rebuilt each model. Surprisingly, all of the cryo-EM densities in both maps could be accounted for by a complex with  $\alpha_2\beta_2\gamma_2D_1$  stoichiometry. These asymmetric complexes were supported by a molar mass estimate, acquired by size-exclusion chromatography coupled with multiangle light scattering, of roughly 256kDa, which is too small for  $\alpha_2\beta_2\gamma_2D_2$  (~313 kDa) and too large for  $\alpha_1\beta_1\gamma_1D_1$  (~157 kDa) (SI Appendix, Fig. S11). Consistent with the hypothesis that McrD assists in the formation of an assembly intermediate, the two conformations differ in their active-site occupancy. Both active sites in the apo-apo model are empty, whereas the semi-apo model contains one empty active site and the other one shows clear density corresponding to the presence of three ligands ( $F_{430}$ , CoM, and CoB) (Fig. 1 C and D).

In each conformational state, McrD is nestled between the  $\gamma$ ,  $\alpha$ , and  $\alpha'$  subunits (semi-apo lettering, Fig. 2A). Residues 10 to 129 of McrD are resolvable in our cryo-EM density and adopt a  $\beta\alpha\beta\alpha\beta$  fold motif. A large loop between the two  $\beta\alpha\beta$  repeats of McrD, composed of residues 47 to 68, extends upward, forming a wedge between the  $\gamma$  and  $\alpha'$  subunits, positioning the bulk of McrD in a region normally occupied by the N-terminal domain of the  $\alpha$  subunit (Fig. 2B). While many diverse protein families contain a doubled  $\beta\alpha\beta$  motif (e.g., ferredoxin-like fold SCOP ID: 2000014), none of the close hits identified using the Dali structural comparison server (22) contain a similar loop between the  $\beta\alpha\beta$  domains. The N-terminal domain of the  $\alpha$  subunit bends down and outward along the  $\beta$ -sheet of McrD, converting Leu<sup>α78</sup>-Arg<sup>α81</sup> into a  $\beta$ -strand (Fig. 2B). Although the C terminus of McrD is partially unresolved in our structures, overlaying the full-length AlphaFold2 prediction reveals that the C-terminal domain contributes to the formation of a small putative tunnel into which the Leu<sup>α78</sup>-Arg<sup>α81</sup>  $\beta$ -strand fits neatly (SI Appendix, Fig. S12). The formation of this  $\beta$ -strand involves a major reorganization of the N-terminal domain of the  $\alpha$  subunit (Fig. 2C). In both conformations, binding of McrD results in large-scale movements of  $\gamma$  and  $\beta$  compared to previous crystal

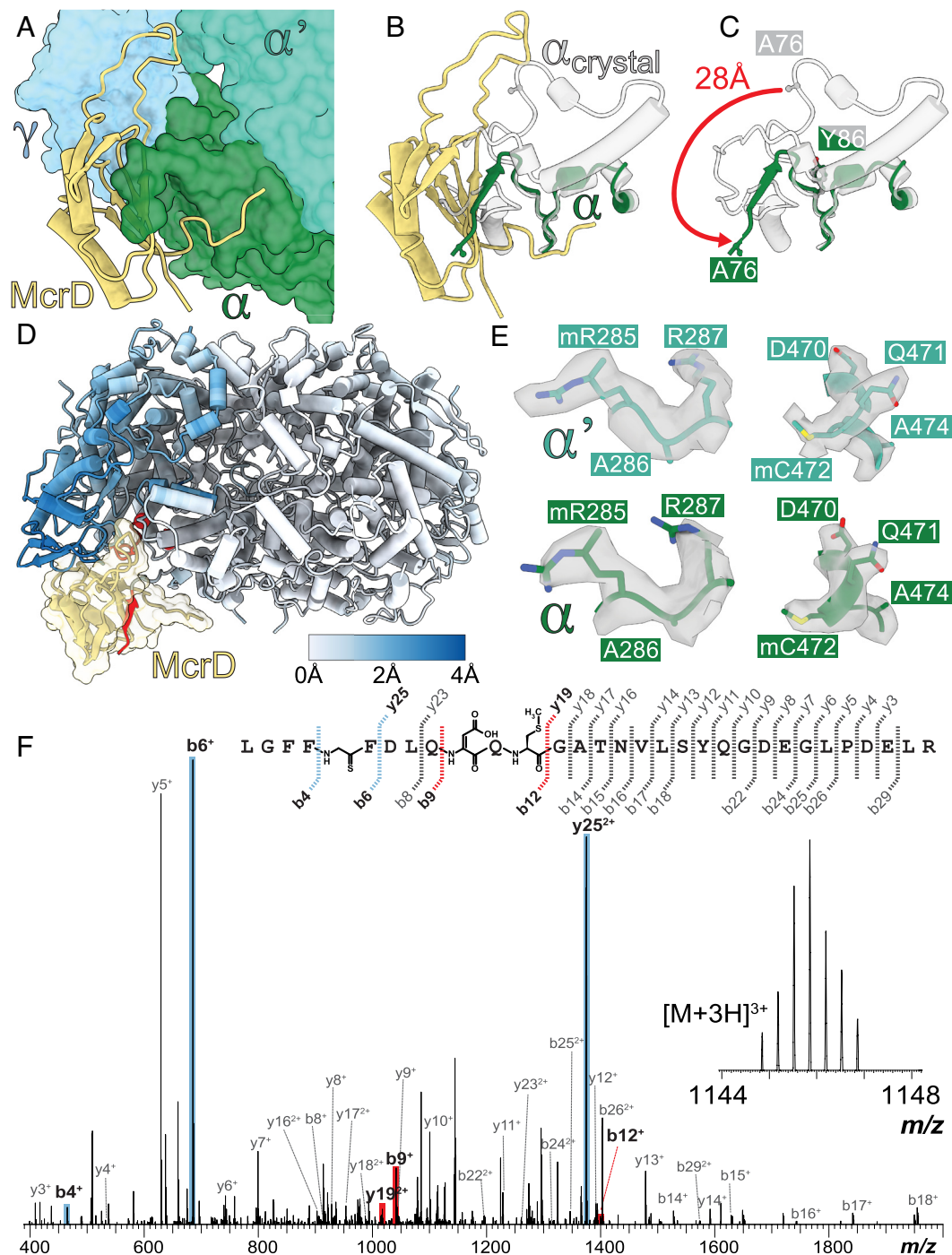


**Fig. 2.** McrD binding to PTM-bearing MCR causes large-scale structural changes. (A) Detail of McrD-binding location on the semi-apo model. (B) The  $\alpha$  subunit N-terminal domain from the *M. barkeri* MCR crystal structure (PDB:1e6y) depicted in white, with the corresponding region of the semi-apo  $\alpha$  subunit in dark green. (C) Significant rearrangement exemplified by Ala<sup>76</sup> which deviates 28Å upon McrD binding. All residues before Ala<sup>76</sup> are unresolved. (D) Ribbon diagram of semi-apo structure colored by C $\alpha$  deviations from 1e6y. Residues deviating by more than the color scale maximum of 4Å are shown in red (Ala<sup>76</sup>-Arg<sup>481</sup>, Tyr<sup>346</sup>-Ala<sup>350</sup>, Pro<sup>409</sup>-Ser<sup>419</sup>), details of which can be found in Fig. 3 and *SI Appendix*, Fig. S15. (E) Density corresponding to methylations at Arg<sup>285</sup> and Cys<sup>472</sup> in the  $\alpha$  and  $\alpha'$  subunits. (F) HRMS/MS fragmentation and annotated collision-induced dissociation spectrum of an McrA tryptic peptide (Leu<sup>461</sup>-Arg<sup>491</sup>) conclusively identified three of the five PTMs. Cyan and red mass peaks indicate the most diagnostic ions for localizing the modification sites. For additional details and HRMS/MS data confirming the remaining PTMs, see *SI Appendix*, Figs. S12–S14.

structures (Fig. 2D), resulting in increased accessibility of the active site on the McrD-bound side. The resolution of the cryo-EM structures was sufficient to visualize the methylations of Arg<sup>285</sup> and Cys<sup>472</sup> in  $\alpha$  and  $\alpha'$  (Fig. 2E), which were also detected by high-resolution and tandem mass spectrometry (HRMS/MS) (*SI Appendix*, Figs. S13–S15). The dihydro Asp<sup>470</sup>, thio Gly<sup>465</sup>, and *N*-methyl His<sup>271</sup> modifications were detected and verified by HRMS/MS despite ambiguity in the cryo-EM data (Fig. 2F).

The asymmetric nature of these structures results in four unique active-site conformations (Fig. 3A and B). In both models, the active site on the McrD-bound side is the most distorted compared to the crystal structure of fully assembled MCR (Fig. 3C and *SI Appendix*, Fig. S16A). Nearly all active site-forming secondary structures deviate significantly and are unresolvable in some places, most notably the loops between Leu<sup>333</sup>-Tyr<sup>346</sup> and Ala<sup>158</sup>-Glu<sup>166</sup> containing the F<sub>430</sub> axial ligand Gln<sup>161</sup>. The loop between Asp<sup>414</sup> and Phe<sup>416</sup>

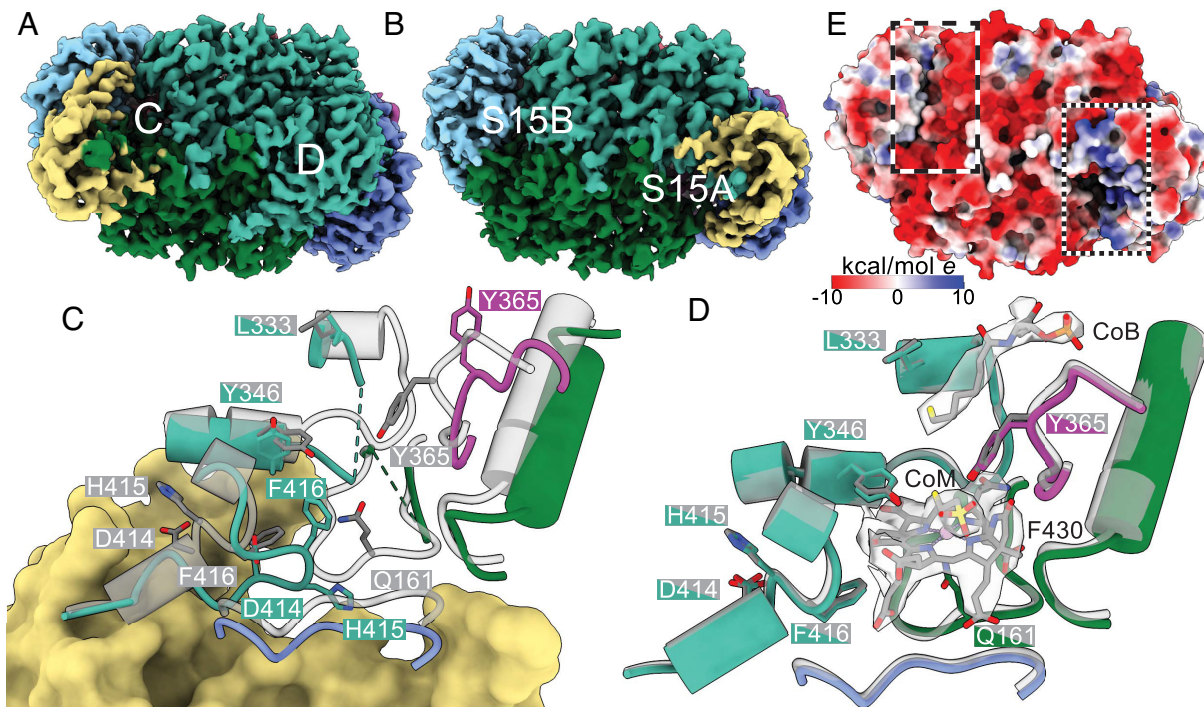


**Fig. 3.** Active-site variations in MCR assembly intermediates. (A and B) Bottom view of semi-apo (A) and apo-apo (B) complexes. Labels indicate subsequent panels and figures in which the active sites are shown in detail. (C and D) Active-site details of the semi-apo model with key residue side chains shown (for corresponding figures for apo-apo model, see *SI Appendix*, Fig. S15). MCR crystal structure from *M. barkeri* (PDB:1e6y) overlaid in gray. In D, cryo-EM density corresponding to CoM, CoB, and F<sub>430</sub> is shown in transparent gray. (E) Bottom view of the apo-apo complex colored by electrostatic potential. Boxed regions on the McrD-bound side (dots) and contralateral side (dashes) highlight strong electrostatic differences, with positively charged patches leading to the active site from McrD and the  $\alpha'$  subunit. Boxes indicate similar positions on the side opposite to McrD with the axial ligand loop blocking the active site and mostly negatively charged surfaces.

shows a dramatic rearrangement, with His <sup>$\alpha 415$</sup>  and Phe <sup>$\alpha 416$</sup>  moving in to occupy regions normally filled by F<sub>430</sub> and the axial ligand loop. Additional structural changes include a distortion to the loop containing Tyr <sup>$\beta 365$</sup> , resulting in a reorientation of the hydroxy group by 180°.

The contralateral active sites differ significantly between the semi-apo and apo-apo states. In the semi-apo complex, the contralateral active site is nearly identical to those observed in the fully assembled crystal structure (Fig. 3D). Strong density is present throughout the entire active-site cavity, allowing for unambiguous identification of CoM, CoB, and F<sub>430</sub> as well as the loop containing Gln <sup>$\alpha 161$</sup> . Here, the N-terminal region of the  $\alpha'$  subunit caps the active site as in the crystal structure. In stark contrast, the contralateral active site of the apo-apo structure displays weak density for the loop with Gln <sup>$\alpha 161$</sup>  and lacks distinct density for the ligands and the entire N-terminal domain of the  $\alpha'$  subunit (*SI Appendix*, Fig. S16B). There is also a prominent deformation of the helix-loop-helix region between Leu <sup>$\alpha 333$</sup>  and Tyr <sup>$\alpha 346$</sup>  that could not be fully resolved. Notably, Gln <sup>$\alpha 161$</sup>  has shifted  $\sim 7$  Å away from the active-site cavity, consistent with a lack of F<sub>430</sub>. A comparison of the two active sites in the apo-apo model highlights the importance of McrD binding for F<sub>430</sub> ingress to the active site. The disordered axial ligand loop leads to a solvent-exposed pathway into the active site that is lined with basic residues contributed by both McrD and the  $\beta$ -strand Leu <sup>$\alpha 78$</sup> -Arg <sup>$\alpha 81$</sup>  (Fig. 3F). In contrast, the contralateral active site remains far less accessible due to a surface covered mostly by acidic residues and an axial ligand loop left largely in place.

## Discussion

Based on these data, we propose a model for the assembly of the MCR complex and the role of McrD in this process (Fig. 4). Our

model begins with a PTM-containing apo- $\alpha_2\beta_2\gamma_2$  MCR that is folded except for the  $\alpha$  subunit N-terminal domains. McrD is not needed to destabilize the  $\alpha$  N-terminal domains, as evidenced by the unstructured contralateral N terminus in our apo-apo  $\alpha_2\beta_2\gamma_2D_1$  structure. Free McrD recognizes one of the unfolded N-terminal domains to bind to the complex, yielding our observed apo-apo  $\alpha_2\beta_2\gamma_2D_1$  state. Though they have never been visualized, there are two hypothetical ways that assembly might proceed: 1) the association of a second McrD on the contralateral side leading to an apo-apo  $\alpha_2\beta_2\gamma_2D_2$  complex, or 2) the insertion of F<sub>430</sub>, dissociation of McrD, and folding of the alpha N-terminal domain to cap the active site producing a semi-apo  $\alpha_2\beta_2\gamma_2$  state. While our purification strategy would never capture the latter state, it should have trapped the former, if present in significant quantities. In the first case, F<sub>430</sub> insertion followed by McrD loss, or in the second case, rebinding of McrD to the opposite side, would lead to our observed semi-apo  $\alpha_2\beta_2\gamma_2D_1$ . From here, an additional round of F<sub>430</sub> insertion, loss of McrD, and folding of the alpha N-terminal domain to cap the active site would yield a conformation identical to the crystallized MCR<sub>ox1-silent</sub> form, which is ready to be a substrate for the activation complex.

Here, we have provided structural insight into the assembly of MCR and McrD's role therein. Similar to the PTMs on the alpha subunit (4), the loss of McrD has little, if any, growth penalty, highlighting that important facets of MCR biology in nature are not captured by ideal laboratory conditions. It seems likely that MCR activity is not growth limiting for *M. acetivorans* under these conditions, which would explain previous results as well as our observation that a decrease to  $\sim 36\%$  of WT F<sub>430</sub> occupancy does not have a more dramatic effect on growth.

McrD is encoded in all genomes containing MCR aside from the anaerobic methanotrophs in the Methanophagales

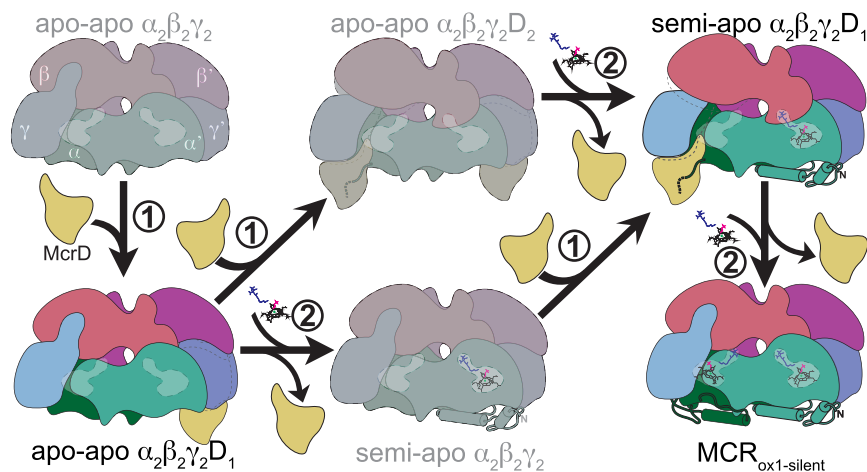


**Fig. 4.** Role of McrD in MCR assembly. Experimentally observed complexes are shown in full color, while hypothesized intermediates are shown in gray. The two proposed functions of McrD are numbered. 1) McrD recognizes the disordered N-terminal domain of an  $\alpha$  subunit lacking  $F_{430}$ , and 2) McrD and possibly unidentified additional factors facilitate the insertion of  $F_{430}$ , McrD dissociation, and  $\alpha$  subunit N-terminal domain folding. The order of these two functions is not clear, leading to two possible routes between our observed assembly intermediates.

(previously ANME-1) (23). The Methanophagales have been shown to utilize a modified form of F430 (6); perhaps, the presence of this modified F430 dispensed the selective pressure to maintain McrD unlike all other methane-metabolizing lineages. In addition, interesting modifications to the McrD primary structure can be found across the diversity of methane-metabolizing archaea (*SI Appendix, Fig. S17*). Notably, a substantial number of sequences have lost all or part of the insertion between the two repeated  $\beta\alpha\beta$  domains which forms the wedge between the  $\gamma$  and  $\alpha'$  subunits. Significant differences can also be found in the length and charge distribution on the unresolved C-terminal domain. Although the  $\beta\alpha\beta\alpha\beta$  fold motif can be found in many diverse protein families, we have been unable to identify any clear McrD homologs in organisms without the remaining MCR subunits, leaving the origin of this protein an unresolved question.

Despite these variations in McrD primary sequence across the archaea, our structural insight into empty MCR active sites could propel the design of unique antimethanogen compounds to block  $F_{430}$  insertion. Potent compounds that inhibit MCR, particularly as additives to ruminant feedstocks (24), will likely be a reliable and cost-effective strategy to curb methane emissions, which is a critical aspect of international efforts to limit global temperature rise. A complete understanding of the MCR enzyme's assembly, activation, and reaction mechanism is crucial for the development and deployment of diverse classes of MCR antagonists. Furthermore, elucidating the process of MCR assembly and activation advances the biotechnological goal of heterologous expression of the methane-generating metabolic pathway and contributes to our comprehension of the evolutionary transitions required for the natural horizontal transfer of this metabolism (25). Future work must identify what additional cellular factors, if any, associate with the McrD-bound assembly intermediates to facilitate  $F_{430}$  insertion and N-terminal domain folding.

## Materials and Methods

**sgRNA Design and Plasmid Construction.** The Cas9 single-guide RNA (sgRNA) sequence used in this study for genome editing was ACCTGATCTCCGATCTGAATAGG (protospacer-adjacent motif (PAM) sequence bold and underlined) and was generated with Geneious Prime v. 11.0. This guide targets the *mcrD* gene (MA4549) and matches 5,600,053-5,600,075 (+strand) in the *M. acetivorans* C2A genome. The

CRISPR site finder tool was used with a PAM site at the 3' end with no off-target matches to the *M. acetivorans* genome allowed. The plasmids and primers used in this study are listed in Supplementary *SI Appendix, Tables S1 and S2* and were generated as previously described (26).

**Growth Media and Mutant Generation.** *M. acetivorans* strains were routinely maintained in 10 mL of high salt (HS) media with either acetate (40 mM), methanol (125 mM), or trimethylamine (50 mM) as the sole carbon and energy source as previously described (27). For transformation, 10 mL cultures in late exponential phase were anaerobically pelleted and subjected to liposome-mediated transformation using established protocols (28). Selection for transformants was carried out on HS media with 50 mM trimethylamine as the carbon source solidified with 1.5% agar and puromycin at 2  $\mu$ g/mL for positive selection. Colonies were screened for the desired mutation (see below) and restructured on plates with 20  $\mu$ g/mL 8-aza-2,6-diaminopurine (8 ADP) for counter selection to remove the genome-editing plasmid and generate the clean deletion strain. Strains carrying tetracycline-inducible *mcrD* variants are permanently maintained in 2  $\mu$ g/mL puromycin to retain the expression plasmid. *M. acetivorans* strains used and generated in this study are listed in *SI Appendix, Table S3*.

**Mutant Validation.** PCR screening of colonies was carried out on whole cells resuspended in nanopure water amplified with GoTaq<sup>®</sup> Green Master Mix (Promega Corporation). Primers were designed to amplify across the McrD gene (GLC073/74) and from within the McrD gene (GLC073/92 and GLC074/91). Positive identification of  $\Delta mcrD$  genotype with no wild-type contamination came from the expected decrease in product size with the 73/74 primer pair, and no product with the 73/92 or 74/91 primer pairs. PCR primers amplifying the Pac gene (VI095/96) were used to validate the loss of genome-editing plasmids by 8 ADP counter selection, or the presence of heterologous expression plasmids. Whole-genome resequencing of the  $\Delta mcrD$  strain was carried out by extracting genomic DNA from 10 mL of stationary-phase culture grown in HS media with trimethylamine using the Qiagen blood and tissue kit (Qiagen, Hilden, Germany). Illumina library preparation and sequencing was carried out at SeqCenter (Pittsburgh, PA). Comparison of the  $\Delta mcrD$  strain to *M. acetivorans* C2A was carried out using the breseq software package (29). Raw reads are deposited in the Sequencing Reads Archive (SRA) and are available under the BioProject PRJNA942038.

For additional methods, please refer to *SI Appendix*.

**Data, Materials, and Software Availability.** Sequencing reads data have been deposited in SRA (PRJNA942038) (30). All study data are included in the article and/or *SI Appendix*. The model coordinates and cryoEM density maps have been deposited in the Protein Data Bank under accession numbers PDB-8GF5 (31) and PDB-8GF6 (32) and Electron Microscopy Data Bank under accession numbers EMD-29978 (33) and EMD-29979 (34).

**ACKNOWLEDGMENTS.** Funding list for D.D.N.: Beckman Young Investigator Award sponsored by the Arnold and Mabel Beckman Foundation, Searle Scholars Program sponsored by the Kinship Foundation, the Rose Hills Innovator Grant, the Packard Fellowship in Science and Engineering sponsored by the David and Lucille Packard Foundation, and the Simons Early Career Investigator in Marine Microbial Ecology and Evolution Grant sponsored by the Simons Foundation. D.D.N. is a Chan Zuckerberg Biohub Investigator. G.L.C. and A.M.N.J. are supported by the Miller

Institute for Basic Research in Science, University of California Berkeley. This work was supported in part by a grant from the NIH (GM097142 to D.A.M.).

Author affiliations: <sup>a</sup>Department of Molecular and Cell Biology, University of California, Berkeley, CA 94720; <sup>b</sup>Department of Microbiology, University of Illinois, Urbana, IL 61801; <sup>c</sup>Carl R. Woese Institute for Genomic Biology, University of Illinois, Urbana, IL 61801; and <sup>d</sup>Department of Chemistry, University of Illinois, Urbana, IL 61801

1. U. Ermler, W. Grabarse, S. Shima, M. Goubeaud, R. K. Thauer, Crystal structure of methyl-coenzyme M reductase: The key enzyme of biological methane formation. *Science* **278**, 1457–1462 (1997).
2. W. Grabarse, F. Mählert, S. Shima, R. K. Thauer, U. Ermler, Comparison of three methyl-coenzyme M reductases from phylogenetically distant organisms: Unusual amino acid modification, conservation and adaptation. *J. Mol. Biol.* **303**, 329–344 (2000).
3. T. Wagner, C.-E. Wegner, J. Kahnt, U. Ermler, S. Shima, Phylogenetic and structural comparisons of the three types of methyl coenzyme M reductase from methanococcales and methanobacterales. *J. Bacteriol.* **199**, e00197–17 (2017).
4. D. D. Nayak *et al.*, Functional interactions between posttranslationally modified amino acids of methyl-coenzyme M reductase in *Methanosarcina acetivorans*. *PLoS Biol.* **18**, e3000507 (2020).
5. D. D. Nayak, N. Mahanta, D. A. Mitchell, W. W. Metcalf, Post-translational thioamidation of methyl-coenzyme M reductase, a key enzyme in methanogenic and methanotrophic Archaea. *eLife* **6**, e29218 (2017).
6. S. Shima *et al.*, Structure of a methyl-coenzyme M reductase from Black Sea mats that oxidize methane anaerobically. *Nature* **481**, 98–101 (2012).
7. C. J. Hahn *et al.*, Crystal structure of a key enzyme for anaerobic ethane activation. *Science* **373**, 118–121 (2021).
8. T. Wongnate *et al.*, The radical mechanism of biological methane synthesis by methyl-coenzyme M reductase. *Science* **352**, 953–958 (2016).
9. E. C. Duin *et al.*, Mode of action uncovered for the specific reduction of methane emissions from ruminants by the small molecule 3-nitrooxypropanol. *Proc. Natl. Acad. Sci. U.S.A.* **113**, 6172–6177 (2016).
10. D. Hinderberger *et al.*, A nickel-alkyl bond in an inactivated state of the enzyme catalyzing methane formation. *Angew. Chem. Int. Ed.* **45**, 3602–3607 (2006).
11. D. Prakash, Y. Wu, S.-J. Suh, E. C. Duin, Elucidating the process of activation of methyl-coenzyme M reductase. *J. Bacteriol.* **196**, 2491–2498 (2014).
12. Z. Lyu *et al.*, Assembly of methyl coenzyme M reductase in the methanogenic archaeon *Methanococcus maripaludis*. *J. Bacteriol.* **200**, e00746–17 (2018).
13. D. Stroup, J. N. Reeve, Association of the *mcrD* gene product with methyl coenzyme M reductase in *Methanococcus vannielii*. *Biochim. Biophys. Acta* **1203**, 175–183 (1993).
14. N. Shao *et al.*, Expression of divergent methyl/alkyl coenzyme M reductases from uncultured archaea. *Commun. Biol.* **5**, 1–11 (2022).
15. K. Zheng, P. D. Ngo, V. L. Owens, X. Yang, S. O. Mansoorabadi, The biosynthetic pathway of coenzyme F430 in methanogenic and methanotrophic archaea. *Science* **354**, 339–342 (2016).
16. R. K. Thauer, Methyl (Alkyl)-coenzyme M reductases: Nickel F-430-containing enzymes involved in anaerobic methane formation and in anaerobic oxidation of methane or of short chain alkanes. *Biochemistry* **58**, 5198–5220 (2019).
17. D. D. Nayak, W. W. Metcalf, Cas9-mediated genome editing in the methanogenic archaeon *Methanosarcina acetivorans*. *Proc. Natl. Acad. Sci. U.S.A.* **114**, 2976–2981 (2017).
18. A. M. Guss, M. Rother, J. K. Zhang, G. Kulkarni, W. W. Metcalf, New methods for tightly regulated gene expression and highly efficient chromosomal integration of cloned genes for *Methanosarcina* species. *Archaea* **2**, 193–203 (2008).
19. D. D. Nayak, W. W. Metcalf, "Chapter Thirteen—Genetic techniques for studies of methyl-coenzyme M reductase from *Methanosarcina acetivorans* C2A" in *Methods in Enzymology, Enzymes of Energy Technology*, F. Armstrong, Ed. (Academic Press, 2018), pp. 325–347.
20. J. Jumper *et al.*, Highly accurate protein structure prediction with AlphaFold. *Nature* **596**, 583–589 (2021).
21. M. Mirdita *et al.*, ColabFold: Making protein folding accessible to all. *Nat. Methods* **19**, 679–682 (2022).
22. L. Holm, Dali server: Structural unification of protein families. *Nucleic Acids Res.* **50**, W210–W215 (2022).
23. G. L. Chadwick *et al.*, Comparative genomics reveals electron transfer and syntrophic mechanisms differentiating methanotrophic and methanogenic archaea. *PLoS Biol.* **20**, e3001508 (2022).
24. A. N. Hristov *et al.*, An inhibitor persistently decreased enteric methane emission from dairy cows with no negative effect on milk production. *Proc. Natl. Acad. Sci. U.S.A.* **112**, 10663–10668 (2015).
25. P. S. Garcia, S. Gribaldo, G. Borrel, Diversity and evolution of methane-related pathways in Archaea. *Annu. Rev. Microbiol.* **76**, 727–755 (2022).
26. D. Gupta, K. E. Shalvarjian, D. D. Nayak, An Archaea-specific c-type cytochrome maturation machinery is crucial for methanogenesis in *Methanosarcina acetivorans*. *eLife* **11**, e76970 (2022).
27. K. R. Sowers, J. E. Boone, R. P. Gunsalus, Disaggregation of *Methanosarcina* spp. and growth as single cells at elevated osmolarity. *Appl. Environ. Microbiol.* **59**, 3832–3839 (1993).
28. W. W. Metcalf, J. K. Zhang, E. Apolinario, K. R. Sowers, R. S. Wolfe, A genetic system for Archaea of the genus *Methanosarcina*: Liposome-mediated transformation and construction of shuttle vectors. *Proc. Natl. Acad. Sci. U.S.A.* **94**, 2626–2631 (1997).
29. D. E. Deatherage, J. E. Barrick, "Identification of mutations in laboratory-evolved microbes from next-generation sequencing data using breseq" in *Engineering and Analyzing Multicellular Systems: Methods and Protocols, Methods in Molecular Biology*, L. Sun, W. Shou, Eds. (Springer, 2014), pp. 165–188.
30. G. L. Chadwick *et al.*, Studying the role of McrD in *Methanosarcina acetivorans*. NCBI BioProject. <https://www.ncbi.nlm.nih.gov/bioproject/PRJNA942038/>. Deposited 8 March 2023.
31. A. M. N. Joiner, G. L. Chadwick, D. D. Nayak, McrD binds asymmetrically to methyl-coenzyme M reductase improving active site accessibility during assembly. *Protein Data Bank*. <https://doi.org/10.2210/pdb8GF5/pdb>. Deposited 21 April 2023.
32. A. M. N. Joiner, G. L. Chadwick, D. D. Nayak, McrD binds asymmetrically to methyl-coenzyme M reductase improving active site accessibility during assembly. *Protein Data Bank*. <https://doi.org/10.2210/pdb8GF6/pdb>. Deposited 21 April 2023.
33. A. M. N. Joiner, G. L. Chadwick, D. D. Nayak, McrD binds asymmetrically to methyl-coenzyme M reductase improving active site accessibility during assembly. *Electron Microscopy Data Bank*. <https://www.ebi.ac.uk/emdb/EMD-29978>. Deposited 21 April 2023.
34. A. M. N. Joiner, G. L. Chadwick, D. D. Nayak, McrD binds asymmetrically to methyl-coenzyme M reductase improving active site accessibility during assembly. *Electron Microscopy Data Bank*. <https://www.ebi.ac.uk/emdb/EMD-29979>. Deposited 21 April 2023.